

# Compact system design based on digital in-line holographic microscopy configuration

**M. Mihailescu**  
mona\_m@physics.pub.ro

National Institute for Research and Development in Microtechnologies, 126 Erou Iancu Nicolae, Bucharest, 077190, Romania

'Politehnica' University from Bucharest, 313 Splaiul Independentei, Bucharest, 060042, Romania

**M. Kusko**

National Institute for Research and Development in Microtechnologies, 126 Erou Iancu Nicolae, Bucharest, 077190, Romania

We present our study regarding a compact system design for cell counting and simultaneous 3D imaging, based on digital in-line holographic microscopy configuration. The system is built around the known experimental configuration which includes a pinhole but we also investigate the configuration with a monomode fiber as a light source. Considered samples consist of a very low concentration of cells in flow in a microchannel. The main challenge in our design is to obtain the digital hologram of one cell on a regular video camera sensor in proper resolution conditions, as opposed to the usual configurations where the aim is to visualize a large area. This fact is possible with shorter distances between pinhole and sample and with pinholes with diameters slightly larger than 1 micron. These can now be realized by considering the microtechnological processes for microchannel and pinhole fabrication on the same substrate with high refractive index - to increase the numerical aperture of the system. The geometrical parameters are established after the numerical analysis of the diffracted field from a single cell and of the entire system numerical aperture values.

[DOI: <http://dx.doi.org/10.2971/jeos.2012.12010>]

**Keywords:** digital in-line holographic microscopy, microchannel, red blood cells, counting, screening, microtechnology

## 1 INTRODUCTION

Starting from Denis Gabor's principle introduced for holography, many branches have since been developed with different applications: digital in-line holographic microscopy [1]-[3], digital off-axis holographic microscopy [4, 5], holographic interferometry [6], holographic memories [7], to name but a few. The main difference between classical holography and new techniques is the recording media. In the case when the holograms are recorded on a video camera sensor, the reconstruction must be performed numerically, using proper algorithms in correlation with the experimental setups, based on the diffraction theory [8, 9].

The digital in-line holographic microscopy (DIHM) technique assumes that a point source illuminates an object. The diffracted beam superposed on the undiffracted beam (which forms the reference beam) is recorded on a CCD camera. For this experimental setup, several configurations have been proposed [10, 11] and adequate algorithms have been developed for object image reconstruction and for its better refocusing criterion [12]-[14]. DIHM configuration offers in the reconstructed function quantitative information along the propagation axis with nanometer accuracy in certain conditions [15]-[18], which completes the transversal dimensions for 3D object images. Furthermore, this technique allows high speed image acquisition suitable for studying cells involved in fast processes like flow in microchannels.

In this paper we present our work developed with the aim

to design a compact system for cell counting and visualization in the same time, based on the DIHM configuration. The motivation started from the idea that in routine automated blood analysis (using impedance counter for example), the number of different blood cell types is established, but their 3D shapes, which are important for the identification of different diseases, cannot be visualized. Because biological samples are transparent in visible light, only when they are combined with chromatographic agents, they can be studied in classical bright field microscopy; otherwise special techniques are necessary, such as phase contrast, differential interference contrast, diffraction phase cytometry [19], holographic microscopy.

We propose a compact system where a low concentration of red blood cells (RBCs) flows in a microchannel which is illuminated by a quasipoint source (which can be defined by a pinhole). The microtechnological progresses offer now the possibility to consider the microchannel and the pinhole on the same substrate (on opposite faces). These lead to a decrease in the pinhole-sample distance and enable small sample volume analysis, with cells inside a medium with high refractive index.

In the design of this system we must meet all optical conditions for a DIHM experimental setup in accordance also with the possibility offered by the microtechnological processes. To satisfy the requirement for simultaneously counting and visu-

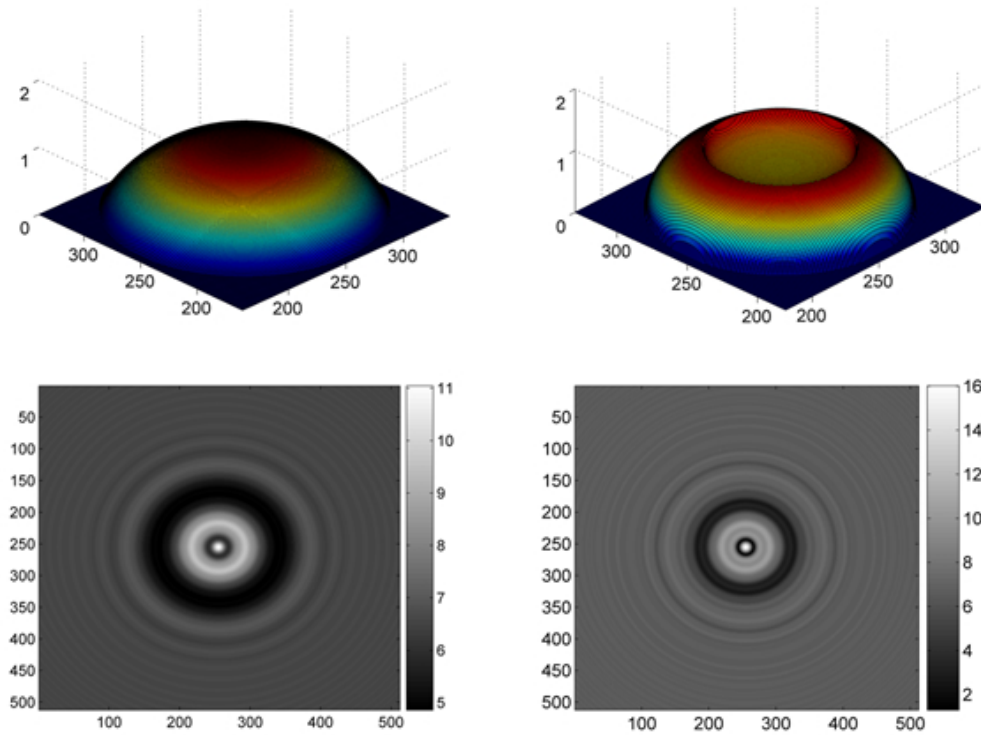


FIG. 1 Modeled shape for a) immature RBC and b) mature RBC; c), d) Diffracted amplitude from cells with phase-only transmission function modeled as a) and b) respectively (all are resized from representation reason).

alization, the system must fulfill some conditions for dimensions and distances. For example, usually in DIHM setups are used pinholes with hundreds of nanometers in diameter for large area illumination. To simulate the case when we visualize each cell separately, in our system we will decrease the distance between the pinhole and the sample plane and also we will consider pinholes greater than 1 micron. But, for these diameters, the numerical aperture (an important parameter for setups in DIHM configuration) decreases. To increase its values, we consider mediums with high refractive index to design the system.

In our simulations we started with analytical dependences between geometrical and optical parameters (pinhole diameter, pinhole-microchannel distance, microchannel-CCD sensor distance, microchannel dimensions, refractive indices) and we looked for finding some intervals for their values to meet satisfied resolution values and to remain inside technological requirements. The diffracted field from different RBC types which flow in a microchannel is obtained at different distances. We also investigated the possibility of using a monomode fiber as a gaussian field source of 3.5  $\mu\text{m}$  in diameter. An optical fiber was also used in other setups for DIHM configuration, but with the aim to visualize a large portion of the sample volume [20].

## 2 DIFFRACTION PATTERN

In the DIHM experimental setup configuration based on a point source, a spherical wave passes through the sample. On the CCD camera is recorded the hologram composed by the superposition between the diffracted and the undiffracted

wave (reference wave). The resolution in the hologram plane and consequently on the image of the reconstructed object is linked with the number and dimension of the recorded fringes, the latter being in turn related to the pixel pitch. Two sample details can be resolved from the whole sample if the number of captured fringes is large (minimum ten fringes) and if one fringe spans a minimum of three camera pixels [21].

Based on these ideas, we calculate the diffraction pattern from each cell types located in the sample using diffraction theory in the Fresnel approximation [22]. In this case, the Fresnel diffraction equation yields the following expression for the diffracted field  $D_F(x_H, y_H)$  in any point  $(x_H, y_H)$  in the hologram plane:

$$D_F(x_H, y_H) = \iint_{\Sigma} h(x_O, y_O, x_H, y_H) T_O(x_O, y_O) dx_O dy_O \quad (1)$$

where the weighting function  $h(x_O, y_O, x_H, y_H)$  depends on the dimensions of diffractive structures and distances between the object plane and the hologram plane (CCD sensor plane). For DIHM geometries with point source, we suppose a nearly spherical incident wave in the object plane, with the usual weighting function from the reference [21] for distances where Fresnel number is very close to 1.

The transmission function  $T_O(x_O, y_O)$  for our samples is computed as being phase only, because biological samples are transparent in the visible range.

$$T_O(x_O, y_O) = \exp(i \cdot \Delta\Phi(x_O, y_O)) \quad (2)$$

where the phase difference introduced by the sample is:

$$\Delta\Phi(x_O, y_O) = \frac{2\pi}{\lambda} [(n_c - n_m)z(x_O, y_O)] \quad (3)$$

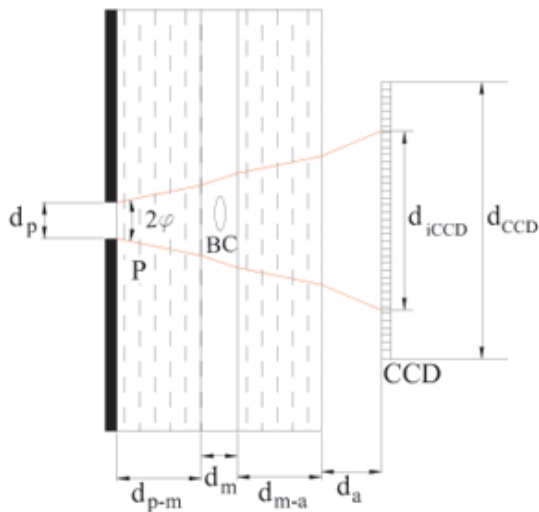


FIG. 2 Sketch of our compact system.

and the refractive index  $n_c$  and  $n_m$  are for cells and the liquid medium which surround them. Their shapes are modeled as oblate spheroids with different characteristics. At every point, the cell thickness,  $z$ , is linked with the coordinates  $(x_0, y_0)$  in a plane perpendicular to the propagation axis, through the equation of the centered ellipsoid in the Cartesian coordinate system:

$$\frac{x_0^2}{a^2} + \frac{y_0^2}{b^2} + \frac{z^2}{c^2} = 1 \quad (4)$$

where  $a$  and  $b$  are the equatorial radii and  $c$  is the polar radius. Immature RBCs are simple oblate spheroids with circular projection. Mature RBCs are biconcave oblate spheroids with circular projection. Two of them are represented in false color in Figure 1(a) and (b), like normalized phase distribution. The diffracted amplitude (transversal section) is obtained at different distances. In Figure 1(b), (c) are presented two of these sections (cropped 10 fringes from central region) at  $z = 1$  mm, when we modeled the immature RBC like oblate spheroids with diameter in equatorial axis  $9 \mu\text{m}$  and in polar axis  $4 \mu\text{m}$ , mature RBC like oblate spheroids with diameter in equatorial axis  $7 \mu\text{m}$  and in polar axis  $2.5 \mu\text{m}$  with a concavity of  $4 \mu\text{m}$  in equatorial axis and  $1 \mu\text{m}$  in polar axis. The refractive indices are considered constants at mean values from the literature: 1.39 and 1.41 for immature and mature RBC respectively [23]-[25].

All these simulations are performed with the aim of knowing the diameters of the diffraction patterns which fulfill the resolution constraints on the CCD sensor in accordance with the equipment features. The maximum value for the spatial frequency which is resolvable by a digital detector  $f_{\text{max}} = 1/2\delta$  is inversely proportional with the pixel pitch distance,  $\delta = 7.4 \mu\text{m}$  in the case of our Kodak sensor.

### 3 COMPACT SYSTEM DESIGN

Two different configurations exist for the DIHM experimental setup with point source: Eq. (1) introduced by Kreuzer's and his team [26], Eq. (2) introduced by Ozcan and his collab-

orators [27]. The main idea for both configurations is based on Gabor's consideration to introduce a pinhole, but the distances (pinhole to sample and sample to CCD sensor) are in different ranges. A sketch of our designed setup is shown in Figure 2; the compact system includes a microchannel with thickness  $d_m$  in polydimethylsiloxane (PDMS) or SU8 photoresist deposited on a glass substrate and a pinhole on the other side of the same glass slide. The plane situated in the middle of the microchannel, parallel with the CCD sensor plane we call it the microchannel axial plane, where we placed the cells in our simulations.

From this punctual source, a spherical wave propagates within a cone, which has the half angle of:

$$\sin \varphi = 1.22 \frac{\lambda}{d_p} \quad (5)$$

where  $d_p$  is the pinhole diameter and  $\lambda = 635 \text{ nm}$  is the used wavelength from a laser source. In the case of our setup (Figure 2), we make the following notations:  $d_{p-m}$  - the distance between the pinhole and the microchannel,  $d_m$  - the microchannel width,  $d_{m-a}$  - the distance between the microchannel and the air surface,  $d_a$  - the distance between the air surface and the CCD camera sensor.

An important parameter of the DIHM setup in this lensless configuration, which establishes the quality of the reconstructed object image, is the numerical aperture (NA) of the entire system. It depends on the distance between the pinhole and the CCD camera sensor and on the CCD camera aperture [28]:

$$NA = \frac{d_{CCD}/2}{\sqrt{(d_{CCD}/2)^2 + (d_{p-m} + d_m + d_{m-a} + d_a)^2}} \quad (6)$$

where  $d_{CCD}$  is the diameter of the active area of the CCD sensor (detector width).

When the medium passed by the beam isn't simple air, we must calculate the expression for the effective wavelength [17]:

$$\lambda_{eff} = \frac{\lambda}{n} \quad (7)$$

where  $n$  represent the refractive index of the passed medium. In our system, different portions passed through the laser beam are made from different materials. In this case, in literature [17] is introduced the effective refractive index  $n_{eff}$ . The effective wavelength becomes:

$$\lambda_{eff} = \frac{\lambda}{n_{eff}} = \frac{\lambda (d_{p-m} + d_m + d_{m-a} + d_a)}{d_{p-m}n_{glass} + d_m n_m + d_{m-a}n_{glass} + d_a} \quad (8)$$

where  $n_{glass} = 1.5$ ,  $n_m = 1.34$  are the refractive indices for glass substrate, for the fluid medium within the microchannel, respectively. In this case, also the numerical aperture of the system increases with a factor  $n_{eff}$  [17].

The geometrical design of our compact system must take into account many interrelated parameter values linked with: cell diameter, pinhole diameter, diffraction pattern shape and dimension from a single cell, microchannel dimensions and geometry, axial distances, refractive indices of employed materials, illuminated area on the CCD camera sensor. An extended

analysis of parameters for DIHM setup was done by Garcia-Sucerquia et al. [28], in the usual case, when a large field of view is concerned. However, for an integrated system which is used in specific conditions, a special design is needed [29].

Our idea to visualize small volume is based on the fact that now, the microtechnological processes permit pinhole fabrication on the same substrate with the microchannel. In this way, we eliminate the distance through air after the pinhole which leads to decrease values for the pinhole-sample distance. Consequently, the optical path values through high refractive index medium increases which leads to increase the system NA. In [17] the researchers increase the NA value in DIHM configuration using particles immersed in oil with high refractive index. Recently another configuration was also reported [16] for NA=0.8 in DIHM, achieved with air between the pinhole and sample to visualize a large area from the sample. The values for NA are inverse proportional with the pinhole diameter.

The NA parameter is important because the resolution is also related with it:

i) The lateral resolution - the minimum distance to which the system distinguishes two neighboring points [28]:

$$\Delta_{lat} = \frac{\lambda}{2 \cdot NA} \quad (9)$$

ii) The depth resolution [30]:

$$\Delta_{long} = \frac{\lambda}{2(NA)^2} \quad (10)$$

In order to increase the resolution in systems based on the DIHM configuration, an idea based on different angles for illumination was recently introduced [18], but this is unsuitable for dynamic samples because two images in two different conditions are needed for the same sample.

Some other conditions must be taken into account in order to design our compact system for cell visualization and count: Eq. (1) in order to avoid multiple cell superposition in flow in the microchannel, its thickness is considered in the range 30-40  $\mu\text{m}$  Eq. (2) in order to record on the CCD camera sensor the hologram of a single cell, we must choose a proper value for the cone angle with its top on the pinhole Eq. (3) the area occupied by the cell must be less than approximately half from the illuminating area in the sample plane [20]. For these reasons, we consider the dependence between the pinhole diameter and the distance  $d_{p-m}$  for different cell diameters (between approx. 7-11  $\mu\text{m}$ ) and respective illuminating area of the cell (between approx. 20-36  $\mu\text{m}$ ) in the microchannel axial plane. (These values are considering for a lower limit. For cells with larger diameters, the distances will be greater). Figure 3 shows several curves regarding these parameters when we consider that the illumination cone 'sees' only one cell. The condition that the pinhole-sample distance must be greater than  $\sqrt{2}/2$  from the geometrical dimension of the sample [12] is satisfied in all cases for  $d_{p-m} > 100 \mu\text{m}$ .

In order to establish the microchannel-air distance we must take into account the NA values. First, we correct the theoretical relation because is obvious that not all the CCD camera

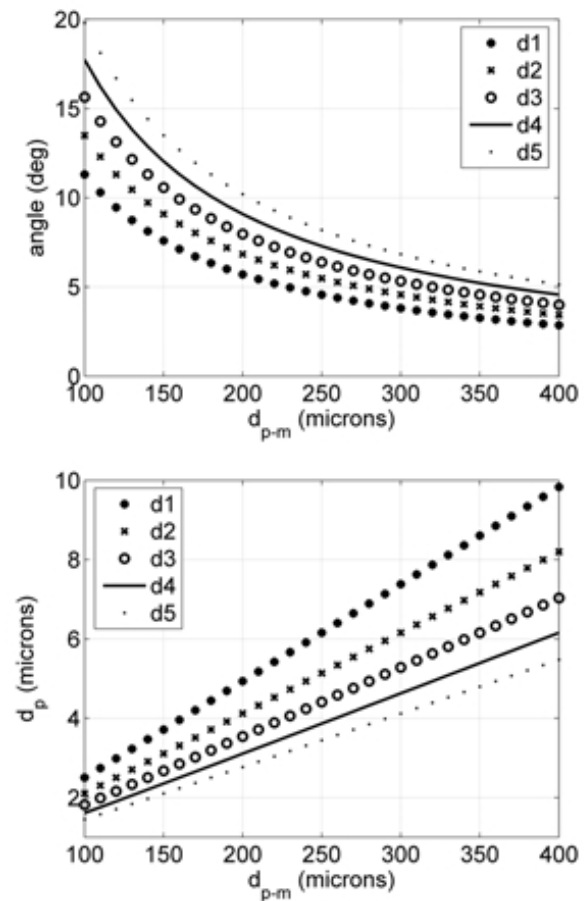


FIG. 3 a) Illumination cone angle vs. pinhole-microchannel distance b) Pinhole diameter vs. pinhole-microchannel distance for different illumination area diameters  $d_1=20 \mu\text{m}$ ,  $d_2=24 \mu\text{m}$ ,  $d_3=28 \mu\text{m}$ ,  $d_4=32 \mu\text{m}$ ,  $d_5=36 \mu\text{m}$  in the microchannel axial plane.

sensor will be covered by the laser wavefront (the detector is not fully illuminated). We computed the adequate values for illuminated  $d_{iCCD}$  in different conditions for each set of interrelated geometrical parameters, with the aim to appear the hologram of one cell on the CCD camera sensor. For example, starting with an angle of around 14 degrees, the illumination zone on the CCD sensor will be 2.2 mm in diameter and in this case the geometrical path between the point source and the CCD camera sensor must be 4.4 mm (in air). Using materials with high refractive index, the distance to the CCD camera sensor will be shorter. In Fig.4 are presented the curves for NA values dependence with  $d_{p-m}$  for different combination between the distances  $d_{m-a}$  and  $d_a$  so as to fulfill the previous conditions.

In all cases, the NA values are within usual ranges for this technique, using normal values for the geometrical parameters; they can be increased using smaller wavelengths and some higher refractive index materials transparent for visible wavelengths (the CCD cameras are cheaper in this range).

Because in DIHM a single hologram, acquired in fractions of a second, contains information about the entire path traveled by the laser beam, for depth resolution values we have no supplementary restriction in our system. Different planes with details from the object domain are distinguished by choosing different values for longitudinal distance (along propagation

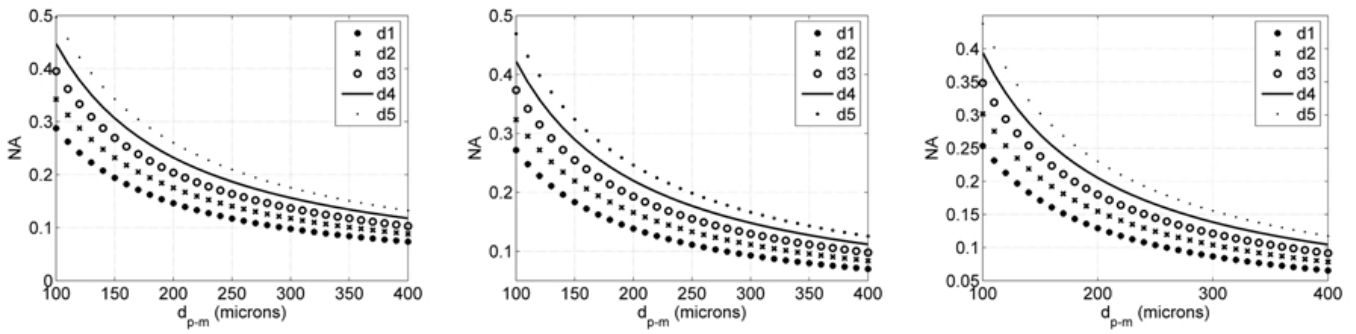


FIG. 4 a) Fig.4 Dependence for NA values vs. pinhole-microchannel distance at a)  $d_{m-a}=2.2$  mm  $d_a=0.5$  mm, b)  $d_{m-a}=2$  mm  $d_a=1$  mm, c)  $d_{m-a}=2$  mm  $d_a=2$  mm, for different illumination area diameters  $d_1=20\mu\text{m}$ ,  $d_2=24\mu\text{m}$ ,  $d_3=28\mu\text{m}$ ,  $d_4=32\mu\text{m}$ ,  $d_5=36\mu\text{m}$  in the microchannel axial plane.

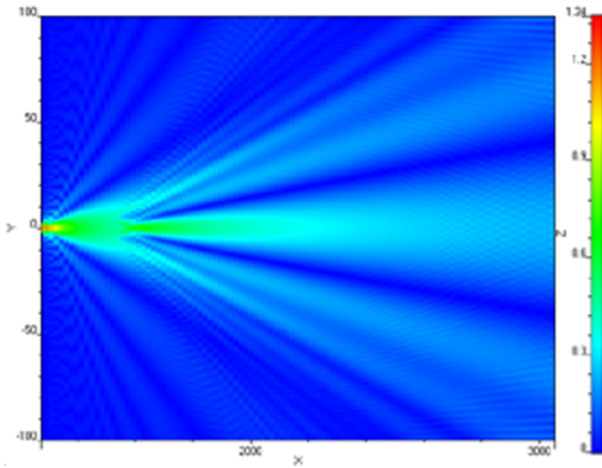


FIG. 5 Section in xOz plane of the propagated field in BPM.

axis) in the algorithm of the reconstruction process or by employing a refocusing algorithm [14].

### 4 NUMERICAL RESULTS

The system geometry was implemented using OptiBPM software [31] based on Beam Propagation Method, which is dedicated package software for photonic integrated circuits but it can be also used for simulation of other optical configurations like microsystems including optical microfluidic circuits. In Figure 5 is a section in xOz plane of the propagated field through the system. The source is considered the pinhole in the left side. The field propagation is simulated through the glass substrate, the microchannel where is diffracted on an RBC, through the glass cover layer, and finally through air to the screen (the CCD-right side).

The simulations were performed in different geometrical conditions. From now on, we consider two cases for the illumination source: Eq. (1) a pinhole with a diameter of  $d_p=5\mu\text{m}$  on one face of the glass support, Eq. (2) the exit of a monomode fiber with the mode field diameter of  $d_f=3.5\mu\text{m}$ . On the opposite face of the glass slide, we consider the microchannel manufactured in PDMS or SU8 photoresist (width  $30\mu\text{m}$ ). The parameters for cells geometry are: immature RBC is considered an oblate spheroid with  $2\mu\text{m}$  polar radius,  $4.5\mu\text{m}$  equatorial radius, 1.39 refractive index, mature RBC is considered an oblate spheroid with  $1.218\mu\text{m}$  polar radius,  $3.5\mu\text{m}$  equatorial

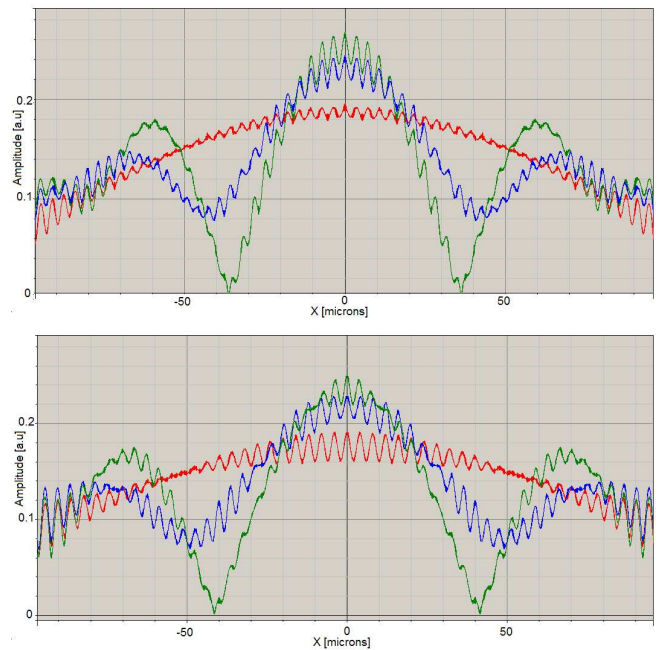


FIG. 6 Amplitude profiles from: simple liquid in microchannel (red), immature RBC (green), mature RBC (blue) in configuration with  $d_p=5\mu\text{m}$ ,  $d_{p-m}=250\mu\text{m}$ , a)  $d_{m-a}=800\mu\text{m}$   $d_a=0.5$  mm b)  $d_{m-a}=1$  mm,  $d_a=0.5$  mm.

radius, 1.41 refractive index, for its concavity we consider the polar radius  $0.5\mu\text{m}$  and equatorial radius  $2\mu\text{m}$ .

In Figure 6 are shown some profiles computed in OptiBPM cut through the middle of the 2D amplitude distribution in the CCD camera sensor plane when we consider the case with pinhole. These amplitude profiles reveal the fact that one can distinguish different types of cells besides the case when the microchannel is empty. We consider that the small fringes at the exit fields after propagation on long distances appear because the radiation reflected at the lateral edges of the computation domain. We choose this pinhole diameter because was demonstrated [32] that this diameter is suitable also with a LED like source from the point of view of intensity, coherence and resolution in the reconstructed object image. This final consideration offers the possibility to change the illumination source after making the system, which leads to a cheaper system and high flexibility in the measurements part.

In this design we also investigate the possibility of replacing the pinhole with the end of a single mode fiber (mode field

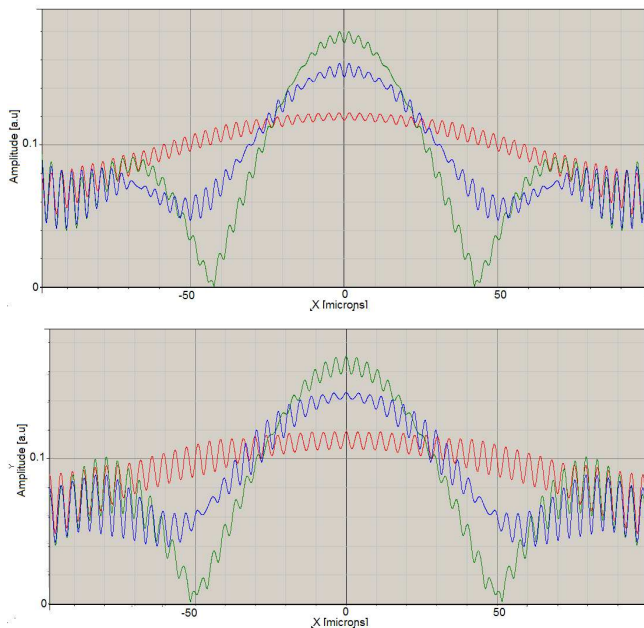


FIG. 7 Amplitude profiles with: simple liquid in microchannel (red), immature RBC (green), mature RBC (blue) in configuration with monomode fiber,  $d_{p-m} = 150 \mu\text{m}$ , a)  $d_{m-a} = 800 \mu\text{m}$ ,  $d_a = 0.5 \text{ mm}$ , b)  $d_{m-a} = 1 \text{ mm}$ ,  $d_a = 0.5 \text{ mm}$ .

diameter  $3.5 \mu\text{m}$ ). In this way, the cost and time required to produce this compact system will be shortened. Also, the lens between the laser and the pinhole will miss. Figure 7 shows several profiles computed in OptiBPM cut through the middle of the 2D amplitude distribution of the diffracted field in the screen plane when we consider a monomode fiber as monopoint source. We chose this representation from comparison reasons, because in this kind the amplitude distributions are clearly differentiated between these three considered cases: empty channel, immature RBC or mature RBC in flow in the microchannel.

## 5 DISCUSSION AND CONCLUSION

We present our design for a compact system with the aim to cell counting and visualization using the digital in-line holographic microscopy principle. All geometrical parameters are studied in detail and all interrelated conditions with optical parameters were analyzed in this computational study. The simulations with different geometrical parameters were performed taking into account the general constraints for in-line holographic setup, for the microchannel and pinhole technological processes and for the refractive indices of common materials used for these purposes.

To choose the proper values we must follow some steps. Starting from information about cell diameter, the illumination diameter in micro channel is chosen and consequently, the cone angle with top in the microchannel and the pinhole diameter is calculated. Linked with these parameters, we find the illuminating area diameter on the CCD camera sensor and the distance between pinhole and CCD camera sensor. Finally, the NA values interval is calculated considering the effective refractive index, for different distances  $d_{m-a}$  and  $d_a$  in order to choose the combination which fulfills all optical, geometrical and microtechnological constraints. Consequently, the com-

compact system design fulfills optical constraints to remain in DIHM domain and to apply common algorithms for 3D object image reconstruction with good enough resolution. This scheme permits computation adaptability starting from many cell types, cell dimension, pinhole diameters, distances in different common materials for different applications.

This analysis shows that a compact system based on the digital in-line holographic microscopy configuration can be designed, manufactured and applied for simultaneous cell count and 3D imaging. Its fabrication is facilitated by the fact that the microtechnological processes (photolithography, thin film deposition, microlithography, etching) permit obtaining on the same glass slide, on opposite faces, of a pinhole and a microchannel. In all cases, the computed NA values are within usual ranges for this technique (between 0.1 and 0.5), using normal values for the geometrical parameters and refractive indices for employed materials.

## 6 ACKNOWLEDGEMENTS

The research presented in this paper is supported by the Sectorial Operational Program for Human Resource Development financed by the European Social Fund and by the Romanian Government under the contract no. POS-DRU/89/1.5/S/63700.

## References

- [1] O. Mudanyali, W. Bishara, and A. Ozcan, "Lensfree super-resolution holographic microscopy using wetting films on a chip," *Opt. Express* **19**, 17378–17389 (2011).
- [2] J. P. Ryle, K. M. Molony, S. McDonnell, T. J. Naughton, and J. T. Sheridan "Multispectral lensless digital holographic microscope: imaging MCF-7 and MDA-MB-231 cancer cell cultures," *Proc. of SPIE* **7442**, 1–11 (2009).
- [3] V. R. Singh, E. Darakis, G. Hegde and A. Asundi, "A new methodology for pixel size retention in lensless digital holographic microscopy applied to micro-particle analysis," *J. Opt.* **13**, 035704 (2011).
- [4] T. Colomb, S. Krivec, H. Hutter, A. A. Akatay, N. Pavillon, F. Montfort, E. Cuche, J. Kühn, C. Depeursinge, and Yves Emery, "Digital holographic reflectometry," *Opt. Express* **18**, 3719–3731 (2010).
- [5] C. Minetti, N. Callens, G. Coupier, T. Podgorski, and F. Dubois, "Fast measurements of concentration profiles inside deformable objects in microflows with reduced spatial coherence digital holography," *Appl. Optics* **47**, 5305–5314 (2008).
- [6] D. D. Aguayo, F. M. Santoyo, M. H. De la Torre-I, M. D. Salas-Araiza, C. Caloca-Mendez, and D. A. G. Hernandez, "Insect wing deformation measurements using high speed digital holographic interferometry," *Opt. Express* **18**, 5661–5667 (2010).
- [7] A. Ogiwara, M. Watanabe, T. Mabuchi, and F. Kobayashi, "Formation of holographic memory for defect tolerance in optically reconfigurable gate arrays," *Appl. Optics* **49**, 4255–4261 (2010).
- [8] M. Kanka, R. Riesenberger, and H. J. Kreuzer, "Reconstruction of high-resolution holographic microscopic images," *Opt. Lett.* **34**, 1162–1164 (2009).
- [9] E. Cuche, P. Marquet, and C. Depeursinge, "Simultaneous amplitude-contrast and quantitative phase-contrast microscopy

- by numerical reconstruction of Fresnel off-axis holograms," *Appl. Optics* **38**, 6994–7001 (1999).
- [10] N. Verrier, C. Remacha, M. Brunel, D. Lebrun, and S. Coëtmelec, "Micropipe flow visualization using digital in-line holographic microscopy," *Opt. Express* **18**, 7807–7819 (2010).
- [11] F. C. Cheong, B. Sun, R. Dreyfus, J. Amato-Grill, K. Xiao, L. Dixon and D. G. Grier, "Flow visualization and flow cytometry with holographic video microscopy," *Opt. Express* **17**, 13071–13079 (2009).
- [12] J. F. Restrepo, and J. Garcia-Sucerquia, "Diffraction-based modeling of high-numerical-aperture in-line lensless holograms," *Appl. Optics* **50**, 1745–1752 (2011).
- [13] S. Coëtmelec, N. Verrier, M. Brunel, and D. Lebrun, "General formulation of digital in-line holography from correlation with a chirplet function," *J. Europ. Opt. Soc. Rap. Public.* **5**, 10027 (2010).
- [14] A. El Mallahi, and F. Dubois, "Dependency and precision of the refocusing criterion based on amplitude analysis in digital holographic microscopy," *Opt. Express* **19**, 6684–6698 (2011).
- [15] I. Moon, F. Yi, and B. Javidi, "Automated Three-Dimensional Microbial Sensing and Recognition Using Digital Holography and Statistical Sampling," *Sensors* **10**, 8437–8451 (2010).
- [16] M. Kanka, R. Riesenberger, P. Petruck, and C. Graulig, "High resolution ( $NA=0.8$ ) in lensless in-line holographic microscopy with glass sample carriers," *Opt. Lett.* **36**, 3651–3653 (2011).
- [17] J. Garcia-Sucerquia, W. Xu, M. H. Jericho, and H. J. Kreuzer, "Immersion digital in-line holographic microscopy," *Opt. Lett.* **31**, 1211–1213 (2006).
- [18] V. Mico, and Z. Zalevsky, "Superresolved digital in-line holographic microscopy for high-resolution lensless biological imaging," *J. Biomed. Optics* **15**, 046027 (2010).
- [19] M. Mir, H. Ding, Z. Wang, J. Reedy, K. Tangella, and G. Popescu, "Blood screening using diffraction phase cytometry," *J. Biomed. Optics* **15**, 027016 (2010).
- [20] P. Amsler, O. Stetzer, M. Schnaiter, E. Hesse, S. Benz, O. Moehler, and U. Lohmann, "Ice crystal habits from cloud chamber studies obtained by in-line holographic microscopy related to depolarization measurements," *Appl. Optics* **48**, 5811–5822 (2009).
- [21] P. Ferraro, A. Wax, and Z. Zalevsky, "Coherent Light Microscopy," Chapter 1 Point Source Digital In-Line Holographic Microscopy, Springer Series in Surface Sciences 46, Springer-Verlag Berlin Heidelberg (2011).
- [22] J. W. Goodman, "Introduction to Fourier Optics," Mc Graw-Hill Book Company, (1968).
- [23] B. Rappaz, A. Barbul, Y. Emery, R. Korenstein, C. Depeursinge, P. J. Magistretti, and P. Marquet, "Comparative study of human erythrocytes by digital holographic microscopy, confocal microscopy, and impedance volume analyzer," *Cytometry Part A* **73**, 895–903 (2008).
- [24] W. Groner, N. Mohandas, and M. Bessis "New Optical Technique for Measuring Erythrocyte Deformability with the Ektacytometer," *Clin. Chem.* **26** (10), 1435–1442 (1980).
- [25] F. M. Gaffney Brit, "Experimental Haemolytic Anaemia with Particular Reference to the Corpuscular Haemoglobin Concentrations of the Erythrocytes," *J. Haematology* **3**, 311 (1957).
- [26] W. Xu, M. H. Jericho, I. A. Meinertzhagen, and H. J. Kreuzer, "Digital In-Line Holography of Microspheres," *Appl. Optics* **41**, 5367–5375 (2002).
- [27] S. Seo, T. Su, A. Erlinger, D. Tseng, and A. Ozcan, "On-Chip Cytometry Using Lensless Digital Holography," in *Conference on Lasers and Electro-Optics/International Quantum Electronics Conference*, OSA Technical Digest (CD) (Optical Society of America, Washington, 2009).
- [28] J. Garcia-Sucerquia, W. Xu, S. K. Jericho, P. Klages, M. H. Jericho, and H. J. Kreuzer, "Digital in-line holographic microscopy," *Appl. Optics* **45**, 836–850 (2006).
- [29] S. K. Jericho, P. Klages, J. Nadeau, E. M. Dumas, M. H. Jericho, and H. J. Kreuzer, "In-line digital holographic microscopy for terrestrial and exobiological research," *Planet. Space Sci.* **58**, 701–705 (2010).
- [30] U. Schnars, and W. P. O. Juptner, "Digital recording and numerical reconstruction of holograms," *Meas. Sci. Technol.* **13**, 85–101, (2002).
- [31] [www.optiwave.com](http://www.optiwave.com)
- [32] L. Repetto, E. Piano, and C. Pontiggia, "Lensless digital holographic microscope with light emitting diode illumination," *Opt. Lett.* **29**, 1132–1134 (2004).